Effect of dopant loading and calcination conditions on structural and optical properties of ZrO 2 nanopowders doped with copper and yttrium

L Khomenkova, O Marchylo, Yu Polishchuk, S Ponomaryov, O Isaieva, I Vorona, L Melnichuk, X Portier, O Melnichuk, N Korsunska

Materials Research Express

PAPER

Effect of dopant loading and calcination conditions on structural and optical properties of ZrO_2 nanopowders doped with copper and yttrium

L Khomenkova[1,2,*], O Marchylo[1], Yu Polishchuk[1], S Ponomaryov[1], O Isaieva[1], I Vorona[1], L Melnichuk[3], X Portier[4], O Melnichuk[3] and N Korsunska[1]

[1] V. Lashkaryov Institute of Semiconductor Physics of the NAS of Ukraine, 41 Prospekt Nauky, Kyiv 03028, Ukraine
[2] National University 'Kyiv-Mohyla Academy', 2 Skovorody str., Kyiv 04070, Ukraine
[3] Nizhyn Mykola Gogol State University, 2 Grafska str., Nizhyn 16600 , Ukraine
[4] CIMAP—CEA, UMR CNRS 6252, UNICAEN, ENSICAEN, 6 Boulevard Marechal Juin, Caen 14050, France
[*] Author to whom any correspondence should be addressed.

E-mail: khomen@ukr.net **and** mov310310@gmail.com

Keywords: ZrO_2, doping, crystalline structure, UV-vis diffused reflectance, Raman scattering, infrared reflection spectroscopy

OPEN ACCESS

RECEIVED
1 December 2023

REVISED
27 March 2024

ACCEPTED FOR PUBLICATION
29 May 2024

PUBLISHED
13 June 2024

Abstract

Undoped, Cu and/or Y doped ZrO_2 nanopowders were synthesized with Zr, Y, and Cu nitrates using a co-precipitation approach. Their structural and optical properties were examined regarding dopant content (0.1–8.0 mol.% of CuO and 3–15 mol.% of Y_2O_3) and calcination conditions (400 °C–1000 °C and, 1,2 or 5 h) through Raman scattering, XRD, TEM, EDS, AES, EPR, UV–vis and FTIR diffused reflectance methods. The results showed that both Cu and Y dopants promoted the appearance of additional oxygen vacancies in ZrO_2 host, while the formation of tetragonal and cubic ZrO_2 phases was primarily influenced by the Y content, regardless of Cu loading. The bandgap of most of the powders was observed within the 5.45–5.65 eV spectral range, while for those with high Y content it exceeded 5.8 eV. The (Cu,Y)-ZrO_2 powders with 0.2 mol.% CuO and 3 mol.% Y_2O_3 calcined at 600 °C for 2 h demonstrated nanoscaled tetragonal grains (8–12 nm) and a significant surface area covered with dispersed Cu_xO species. For higher calcination temperatures, the formation of Cu_{Zr}^{2+} EPR centers, accompanied by tetragonal-to-monoclinic phase transformation, was found. For fitting of experimental FTIR reflection spectra, theoretical models with one, five, and seven oscillators were constructed for cubic, tetragonal, and monoclinic ZrO_2 phases, respectively. Comparing experimental and theoretical spectra, the parameters of various phonons were determined. It was found that the distinct position of the high-frequency FTIR reflection minimum is a unique feature for each crystalline phase. It was centered at 700–720 cm^{-1}, 790–800 cm^{-1}, and 820–840 cm^{-1} for cubic, tetragonal, and monoclinic phases, respectively, showing minimal dependence on phonon damping coefficients. Based on the complementary nature of results obtained from structural and optical methods, an approach for monitoring powder properties and predicting catalytic activity can be proposed for ZrO_2–based nanopowders.

1. Introduction

Zirconia (ZrO_2) is a versatile material available in various forms, such as crystals [1, 2], ceramics [3, 4], films [5], and (nano)powders [6, 7]. ZrO_2 possesses unique mechanical, electrical, thermal, and optical properties, making it suitable for a wide range of applications, including high-temperature and corrosion-resistant coatings, radiation detectors, biological labeling, catalysts, oxygen sensors, and solid-oxide fuel cells [[7] and references therein]. However, for many critical applications, pure ZrO_2 may be insufficient, and its doping or alloying with other metal oxides can be required [1–10]. The addition of complementary cations to the crystal lattice of zirconia can significantly alter its properties [1, 5–7].

One of the crucial parameters affecting ZrO_2 applications is its crystal structure. Pure zirconia in bulk form typically adopts a monoclinic (*m*) crystal structure at room temperature. It transforms into tetragonal (*t*) phase upon heating (around 1460 °C) and into cubic (*c*) phase at higher temperatures. However, it is unstable upon cooling since reverse *c*-*t*-*m* transformation occurs.

For pure ZrO_2 in powder form, especially nanopowders, heating at moderated temperature (400 °C–500 °C) favors formation of *c*- and *t*-phases [6] while further temperature rise (up to 1100 °C) converts them in *m*-phase due to grain growth [3, 6, 7]. This phase is stable upon powders cooling. Since application of powders requires stability of the *t*- and *c*-phases not only at room temperature but also at higher temperatures, doping ZrO_2 with subvalent cations is employed [1–14].

Subvalent additives such as yttrium [1, 2, 6, 11, 12], calcium [8], scandium [9], cerium [6, 10], terbium [6], etc., are typically used to stabilize the *t*- and *c*-ZrO_2 [7, 8, 11]. Yttrium is the most common stabilizing agent because it can remain in ZrO_2 host upon annealing at high temperatures (around 1400 °C). The stabilization of both phases is achieved through the formation of oxygen vacancies required for dopant charge compensation [6].

Besides zirconia stabilization via the formation of oxygen vacancies, subvalent impurities are able to enhance other properties [8–14]. In particular, doping with rare-earth ions results in the appearance of intense luminescence in specific spectral ranges [6, 13, 14]. Doping with copper ions favors the appearance of specific green luminescence [15].

In recent years, ZrO_2 powders with stable *t*- and *c*-phases have attracted considerable attention due to their catalytic properties and larger amount of oxygen vacancies compared to those of *m*-ZrO_2 [16, 17].

To achieve high catalytic activity of the powders, several parameters must be considered, including the surface/volume localization of the dopants, their chemical forms and powder surface area [18, 19]. In this regard, in some studies, the attention also focus on amorphous zirconia because of its superior catalytic performance resulting from a higher surface area [17].

Zirconium oxide powders can be produced using a variety of precursor materials and methods. Compounds containing zirconium, such as Zr hydroxide ($Zr(OH)_4$), Zr oxychloride ($ZrOCl_2$), Zr oxynitrate ($ZrO(NO_3)_2$), Zr sulfate ($Zr(SO_4)_2$) can undergo various chemical reactions [7] or thermal treatments [20] to yield ZrO_2 powders. Additionally, Zr alkoxides and organometallic compounds are also attractive for synthesizing not only ZrO_2 [21] but also ZrC powders [22] via sol–gel processes.

Doping of ZrO_2 with multiple additives (referred to as 'co-doping') becomes more attractive for enhancing catalytic activity. For instance, it has been reported for Y-stabilized ZrO_2 (YSZ) powders doped additionally with Pt [19], Ag [23] or Cu [24–26]. It's worth noting that among metallic dopants, copper is more commonly addressed due to its abundance and low cost.

The simultaneous incorporation of several dopants into the zirconia host induces complex structure transformation. For instance, incorporating copper into Y-doped ZrO_2 powders promotes a reduction of grain size and stabilizes *t*- and *c*-ZrO_2 polymorphs [25]. Additionally, it lowers the temperature of the *t*-*m* phase transformation [26]. Similar effects have been observed for ZrO_2 co-doped with Y and Tb^{3+} [2], Nb and Er^{3+} [27], and V and Y [28].

As mentioned above, precise control over the content, spatial distribution and chemical forms of Cu dopants is crucial for Cu-doped ZrO_2-based catalysts. Copper dopants can be introduced in ZrO_2 powders through impregnation [18, 19] and chemical precipitation [29], enriching mainly the grain surface or near-surface region by copper. Alternatively, co-precipitation allows for simultaneous Cu presence throughout the volume of the grains and on their surface [7, 15, 19, 30, 31].

The effect of copper content on the properties of catalysts is influenced by the nature of Zr precursor. The comparison of the (Cu,Y)-ZrO_2 powders prepared from $ZrOCl_2{\cdot}nH_2O$ [30] and $ZrO(NO_3)_2{\cdot}nH_2O$ salts [15, 31] revealed fewer oxygen vacancies in those from $ZrOCl_2{\cdot}nH_2O$. This was attributed to the simultaneous incorporation of chlorine from the Zr precursor via the formation of Cu-Cl complexes and their integration in Cu-Y-ZrO_2 network during sediments precipitation [15]. An increase of Cu loading leads to the pronounced formation of the Cu-Cl complexes, which act as barriers to the appearance of additional oxygen vacancies because no charge compensation is required for Cu dopant [30]. It is interesting that the presence of residual Cl and C even in pure ZrO_2 was reported in [32] and attributed to incomplete hydrolysis reaction of zirconium ethoxide. This drawback can be overcome by using of $ZrO(NO_3)_2{\cdot}nH_2O$ precursor. The powders prepared for this salt exhibited higher amount of oxygen vacancies, which increased with higher Cu loading [15, 31]. These powders showed the high catalytic activity in CO-PROX reaction attributed to the formation of tetragonal ZrO_2 grains covered by dispersed Cu_xO oligomers. However, the focus of these reports was on the (Cu,Y)-ZrO_2 powders with specific dopant content, namely 3 mol.% of Y_2O_3 and 1 or 8 mol.% of CuO [30, 31]. Nevertheless, a more precise variation of Cu and Y content across a wide range was desirable.

It is evident that a comprehensive investigation into the effect of Cu loading (at fixed Y content) and Y loading (at fixed Cu content) on the various properties of the powders, calcined at different temperatures and durations, requires the preparation and characterization of significant number of samples.

When analyzing powders, various methods are employed, including Transmission Electron Microscopy (TEM), X-ray Diffraction (XRD), Energy Dispersive x-ray (EDX), X-ray photoelectron spectroscopy (XPS), and Auger electron spectroscopy (AES), as well as Fourier-transform Infrared (FTIR), Raman scattering, and Ultraviolet-Visible (UV–vis) spectroscopies. Each method serves distinct aspects of powder characterization, offering unique insights that often complement one another when combined. Indeed, to obtain information about the crystalline structure and chemical composition of doped ZrO_2 grains, TEM, STEM-EDX, XPS, and AES methods can be employed. However, such analyses are time-consuming and costly. Simultaneously, correlating their results with those obtained by other methods, including widely available and low-cost optical methods, can be advantageous for efficient optimization of powder properties. Leveraging established correlations between results from structural and optical methods can facilitate the rapid monitoring of powder properties, with a particular emphasis on utilizing optical methods for further analysis that can provide additional benefits in powder diagnostics.

The objective of this study is twofold. Firstly, to investigate the influence of varying Cu and Y content over wide ranges (0.1–8.0 mol.% CuO and 3–15 mol.% Y_2O_3, respectively), along with calcination temperature (from 400 up to 1000 °C) and duration (from 1 to 5 h), on the structural and optical properties of Cu-ZrO_2, Y-ZrO_2 and (Cu,Y)-codoped ZrO_2 powders prepared from Zr, Y and Cu nitrates by co-precipitation method. Secondly, to introduce infrared reflection spectroscopy as a non-destructive method for express material diagnostics, employing its sensitivity to the crystalline structure and surface complexes. The study differentiates the contributions of *m*-, *t*- and *c*-ZrO_2 phases using developed theoretical models, showcasing their effectiveness in fitting experimental spectra and evaluating the structure of powders as well as the nature of surface complexes.

2. Experimental details

2.1. Reagents

Zirconyl (IV) nitrate hydrate ($ZrO(NO_3)_2{\cdot}6H_2O$, 99.5% (contains up to 4% Hf), Thermo Scientific Chemicals), Yttrium (III) nitrate hexahydrate ($Y(NO_3)_3{\cdot}6H_2O$, 99.9%, Thermo Scientific Chemicals), and copper (II) nitrate trihydrate ($Cu(NO_3)_3{\cdot}3H_2O$, 99.0%, for analysis, Thermo Scientific Chemicals), Ammonium hydroxide solution 25% (NH_4OH, for analysis EMSURE® ISO, Reag. Ph Eur, Merck) were used in the synthesis of undoped and doped ZrO_2-based powders.

2.2. Powder synthesis and calcination

Undoped ZrO_2 powders, as well as their counterparts including Cu-ZrO_2, Y-ZrO_2 and (Cu,Y)-codoped ZrO_2, were synthesized. The quantities of Zr, Cu and Y precursors were adjusted to vary the content of Y_2O_3 and/or CuO in the doped powders across wide ranges, specifically, 3–15 mol. % of Y_2O_3 and 0.1–8.0 mol.% of CuO. The precursors taken in required ratio were dissolved in 100 ml of double-distilled water and magnetically stirred for 2 h at 60 °C until a transparent homogeneous solution was obtained. To induce precipitation, this solution was mixed with a 25% ammonium hydroxide solution, resulting in a gel-like substance.

The chemical reaction for Zr precursor depends on the pH of solution and can follow two pathways:

$$ZrO(NO_3)_2 + H_2O + 2NH_4OH \longrightarrow Zr(OH)_4 + 2NH_4NO_3$$

and

$$ZrO(NO_3)_2 + 2NH_4OH \longrightarrow ZrO(OH)_2 + 2NH_4NO_3.$$

For Y and Cu precursors the reactions are [33]:

$$Y(NO_3)_3 + NH_4OH \longrightarrow Y(OH)_3 + 2NH_4NO_3$$

and

$$Cu(NO_3)_2 + 2NH_4OH \longrightarrow Cu(OH)_2 + 2NH_4NO_3$$

For the production of (Cu,Y)-codoped powders, the global reaction is:

$$ZrO(NO_3)_2 + Y(NO_3)_3 + Cu(NO_3)_2 + 15H_2O + 7NH_4OH \longrightarrow Zr(OH)_4 + 2Y(OH)_3 + Cu(OH)_2 + 7NH_4NO_3$$

However, the balanced reaction depends on the desired composition of the final materials. In our case, the amount of each solution was adjusted to achieve the required composition of the final product as mentioned above.

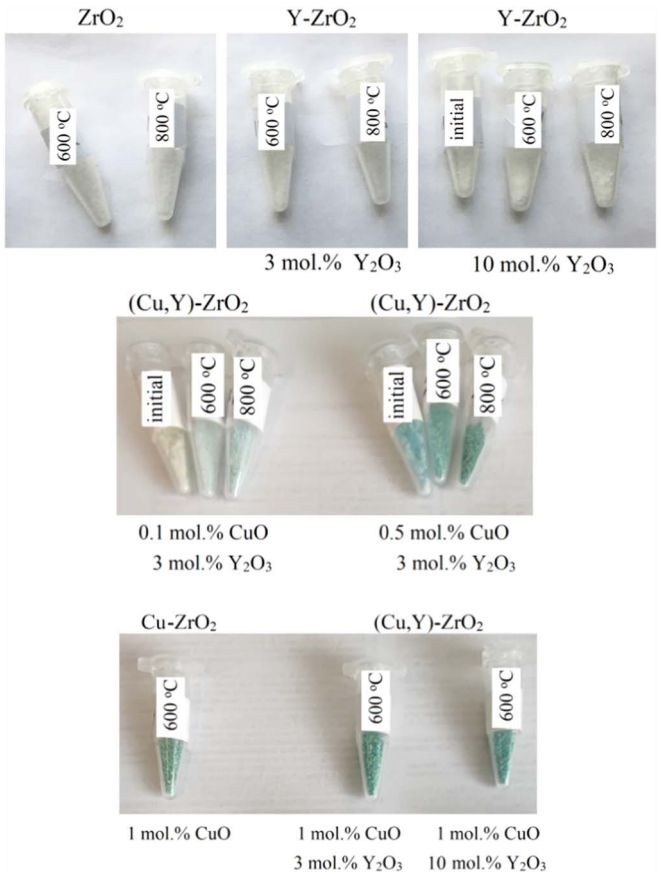

Figure 1. Daylight photo of pure, Y-doped, Cu-doped, and (Cu,Y)-codoped ZrO_2 powders with different dopant content before (initial) and after calcination at 600 or 800 °C for 2 h. The content of Cu and Y dopants is mentioned in the figures.

When the gel-like substance was obtained, it was dried at 80 °C for 48 h to remove water molecules and subsequently heated at 150 °C for 24 h to complete the process. The resulting sediments underwent further calcination at temperatures ranging from $T_c = 400$ to 1000 °C for durations of $t_c = 1$, 2, or 5 h.

The calcination at high temperatures of Zr, Y and Cu hydroxides results in the formation of corresponding oxides

$$Zr(OH)_4 \xrightarrow{T_C,t_c} ZrO_2 + 2H_2O\uparrow$$

$$2Y(OH)_3 \xrightarrow{T_C,t_c} Y_2O_3 + 3H_2O\uparrow$$

$$Cu(OH)_2 \xrightarrow{T_C,t_c} CuO + H_2O\uparrow$$

For (Cu,Y)-codoped ZrO_2 the calcination results in the formation of complex oxide via reaction

$$xZr(OH)_4 + 2yY(OH)_3 + zCu(OH)_2 \xrightarrow{T_C,t_c} (Cu, Y)-ZrO_2 + H_2O\uparrow,$$

where final product (Cu,Y)-ZrO_2 may be considered as a network with zCuO-$y$$Y_2O_3$-$x$$ZrO_2$ composition. As for the ZrO_2 powders doped with one element, either Cu or Y, the final reactions are similar. The calcination conditions determined spatial distribution of these elements.

In this study, ZrO_2 and Y-doped ZrO_2 powders were colorless, while Cu-doped powders were of different blue-green colors under daylight illumination as shown in figure 1 for some powders. Their coloration enhanced after the calcination procedure.

2.3. Methods for materials characterization

The structural and optical properties of the powders were analyzed by means of Raman scattering, X-ray diffraction (XRD), Transmission Electron Microscopy (TEM), Energy dispersive spectroscopy (EDS), Auger electron spectroscopy (AES), Electron Paramagnetic Resonance (EPR), UV–vis diffused reflectance, and FTIR reflection spectroscopy.

Raman scattering spectra were obtained in backscattering geometry using a 785-nm Preconfigured Raman Spectrometer System (StellarNet Inc., USA). The system included a 785 nm Ramulaser Raman laser with

adjustable power (0–499 mW), the Raman-HR-TEC-785 thermo-electrically cooled Raman spectrometer with 4 cm^{-1} resolution and high sensitivity, and a Raman probe that allowed a laser spot of 0.15 mm in diameter on the sample surface. The laser power density on the sample was always kept low to prevent property modifications. Spectra were recorded with an integration time of 15 s and 5 times averaging for each spectrum. The polarization of the scattered light was not analyzed.

X-ray Diffraction (XRD) patterns were acquired in Bragg–Brentano geometry using a Philips X'Pert-MRD diffractometer equipped with CuKα_1 ($\lambda = 0.15406$ nm) radiation source. The data were collected in the range of $2\theta = 20°$–$80°$ with a scanning step of 0.03° to ensure accurate measurements.

Conventional transmission electron microscopy (TEM) and high-resolution transmission electron microscopy (HRTEM) observations were performed using a double-corrected cold FEG JEOL ARM 200 F microscope operated at 200 kV. The powder was stirred with n-butanol, and a drop of the resulting liquid was deposited on a 3 mm diameter copper grid (300 mesh) covered by a holey carbon film. The digitized images were acquired and processed using the commercial DigitalMicrograph software from GATAN.

Auger electron spectroscopy (AES) study was performed using an Auger microprobe JAMP 9500 F (JEOL) tool, provided a 3 nm resolution in secondary electron image mode. The microprobe features a sensitive hemispheric Auger spectrometer with energy resolution ($\Delta E/E$) ranging from 0.05 to 0.6%, along with an ion etching gun for layer-by-layer analysis. The Ar+ ion beam diameter is 120 μm, capable of rastering at 1 × 1 mm. The Ar^+ ion energy range varies from 0.01 up to 4.0 keV, with a minimum beam current of 2.0 μA at 3.0 keV. The specimen chamber maintains a vacuum better than 5×10^{-7} Pa. Additionally, the procedure of thermal drift correction was used during Auger spectra recording because of dielectric nature of the powders. Quantitative element analysis was conducted by calibrating relative sensitivity factors (RSF) on homogeneous reference samples of known compositions.

UV–vis diffuse reflectance spectra ranging from 220 to 1000 nm were recorded using a SilverNova spectrometer equipped with TE-cooled CCD detector (StellartNet Inc., USA) with respect to Spectralon® White Diffuse Reflectance Standard (99%) (Edmund Optics®). The recorded spectra were transformed to the absorption spectra using Spekwin32 software associated with this setup and further analyzed with SpectraGryph software, both created by Dr Friedrich Menges (http://spectroscopy.ninja).

Electron paramagnetic resonance spectra were obtained using the upgraded X-band Varian E-12 spectrometer (~9.5 GHz) with the sensitivity limit of about 10^{12} EPR centers. The spectra were recorded in respect to the signal intensity from a MgO:Mn standard. All EPR spectra were normalized on the mass of the investigated powders.

Infrared reflections spectra were collected over the 200–4000 cm^{-1} range (with a 1 cm^{-1} resolution) using an IRTracer-100 Fourier Transform Infrared Spectrophotometer equipped with a DRS-8000A diffuse reflectance tool (Shimadzu Company, Japan).

All experiments were performed at room temperature.

3. Results and discussion

This section examines the structural properties of both undoped and doped ZrO_2 powders versus dopant content and calcination conditions. Subsequently, their correlation with the optical absorption spectra is explored. Finally, theoretical modelling of the infrared reflection spectra of various ZrO_2 phases is introduced to demonstrate its utility for fitting experimental data as a non-destructive approach for materials characterization.

3.1. Raman scattering and XRD study

3.1.1. Pure ZrO_2 powders

The shape of Raman scattering spectra of ZrO_2–based powders significantly depends on their crystalline structure. Monoclinic ZrO_2 exhibits multiple narrow phonon bands corresponding to nine A_g modes, centered at 302, 344, 473, 553, 633, and 706 cm^{-1}, and six B_g modes, peaking at 219, 330, 378, 499, 533, and 610 cm^{-1} [34, 35]. Tetragonal ZrO_2 shows phonon modes centered at 259, 330, 612, and 636 cm^{-1} [36], while cubic ZrO_2 has broader phonons peaked at 263, 450, and 615 cm^{-1}. The spectral positions of all these phonons may vary depending on the Zr precursor and fabrication procedure [20, 22, 29, 32], while being in the vicinity of numeric values already mentioned.

Typically, undoped ZrO_2 has a monoclinic structure. However, some studies on undoped ZrO_2 nanopowders have reported the presence of a tetragonal and/or cubic structure at room temperature [6, 37]. In this case, ZrO_2 particles were smaller than 10 nm, and the stabilization of both phases was achieved due to high surface/volume ratio and high surface-induced tensions. Annealing of such powders at high temperatures caused grain sintering, followed by an increase in sizes and a decrease of their surface/volume ratio, resulting in the transformation of tetragonal structure to monoclinic [37].

The Raman scattering spectra of pure ZrO_2 powders prepared in this study are presented in figure 2(a). It is seen that after drying at 150 °C for 24 h, only a peak near 1040–1050 cm^{-1} was observed, which was attributed to amorphous Zr hydroxide. The intensity of this peak decreased significantly after powder calcination at $T_c = 400$ °C–500 °C for 2 h, and for higher T_c, no such signal was observed. The powders calcined at $T_c = 600$ °C–700 °C exhibited a significant contribution of Rayleigh scattering, potentially caused by the presence of softly-bound agglomerates of the particles. This hindered the registration of the Raman signal from ZrO_2 grains. In contrast, the Raman signal of the ZrO_2 powder calcined at $T_c = 800$ °C has well-defined phonons. Most of these phonons coincided with those mentioned above for tetragonal phase, while the presence of phonons at 533 and 553 cm^{-1} indicated the appearance of the monoclinic phase. Additionally, the significant presence of Rayleigh scattering suggested the nanocrystalline nature of these powders.

The increase in calcination temperature up to $T_c = 900$ °C promotes pronounced crystallization of the powder. Both tetragonal and, in larger extent, monoclinic phases are observed. Subsequently, calcination at $T_c = 1000$ °C results in complete *t-m* transformation. These findings are corroborated by XRD analysis of the same samples.

For the powders calcined at $T_c < 600$ °C, no XRD reflexes were detected, indicating their amorphous or nanocrystalline nature. Powders calcined at $T_c = 600$ °C exhibited XRD peaks at $2\theta \approx 30.3°$ and 35.2°, and, with lower intensity, at $2\theta \approx 28.2°$ and 31.5°. The two first peaks are considered a characteristic of cubic and tetragonal ZrO_2 phases, while two others are attributed to the monoclinic one.

To distinguish the contributions of cubic and tetragonal phases, analysis of the XRD patterns in the range of $2\theta = 72°–76°$ can be conducted. A single symmetric peak is indicative of the formation of the cubic phase, whereas two peaks near $2\theta = 73.2°$ and 74.6° (or one asymmetric broad peak covering this range) are characteristic of the tetragonal phase.

As depicted in figure 2(c), for $T_c = 600$ °C, two XRD peaks are detected in the range of $2\theta = 72–76°$, providing evidence of the formation of tetragonal ZrO_2. The analysis of lattice parameters yielded values of $a = 0.3592$ nm, $b = 0.3592$ nm, and $c = 0.5179$ nm for *t*-ZrO_2 coinciding with the tabulated data (ICDS card 96–153–9832). The peaks at $2\theta \approx 28.2°$ and 31.5° belong to the monoclinic phase, but its contribution is significantly lower, allowing us to conclude that the main contribution is given by the tetragonal phase in the powders calcined at 600 °C.

At higher T_c, the intensities of the peaks at $2\theta \approx 30.3°$, 35.2°, 73.2° and 74.6° decrease, indicating a reduction in the contribution of tetragonal phase at $T_c = 700$ and 800 °C (figures 2(b), (c)). Additionally, the magnitudes of the peaks at $2\theta \approx 28.2°$ and 31.5° increase (figure 2(b)), along with those appearing in the range of $2\theta = 68–76°$ (figure 2(c)).

All these peaks belong to the monoclinic ZrO_2 phase with lattice parameters $a = 0.5120$ nm, $b = 0.5216$ nm, $c = 0.5281$ nm, $\alpha = 90.000°$, $\beta = 99.010°$ and $\gamma = 90.000°$ (ICDS card 96-900-5834). This phase becomes noticeable at $T_c = 800$ °C. Its contribution continues to increase with the rise in calcination temperature, and for $T_c = 1000$ °C, the monoclinic ZrO_2 phase with lattice parameters $a = 0.5149$ nm, $b = 0.5202$ nm, $c = 0.5323$ nm, $\alpha = 90.000°$, $\beta = 99.164°$ and $\gamma = 90.000°$ (card 96-230-0545) becomes dominant. It is worth pointing out that the half-width of the reflexes decreases with T_c rise, indicating the enlargement of the coherent domain size (d) and the growth of the ZrO_2 grains from $d \sim 10$ nm ($T_c = 600$ °C) up to $d \sim 27$ nm ($T_c = 1000$ °C). Thus, these XRD data show the transformation of the tetragonal phase to the monoclinic one (figures 2(b), (c)) and support the conclusion drawn from Raman scattering data (figure 2(a)).

3.1.2. Doped ZrO_2 powders

Raman scattering spectra of Y-doped ZrO_2 powders with various Y content are depicted in figure 3. These spectra reveal that in Y-ZrO_2 powders with low Y loading (3 mol.% Y_2O_3) calcined at $T_c = 700$ °C–1000 °C, the tetragonal ZrO_2 phase is present and remains stable at high temperatures (figures 3(a), (b)). Interestingly, for the powders calcined at $T_c < 700$ °C, the cubic ZrO_2 phase was detected.

At higher Y loading (8–15 mol.% Y_2O_3), only the cubic phase is observed regardless of calcination temperature and duration (up to 5 h) (figure 3(b)). However, a peak at 485 cm^{-1} is still detected, indicating a mixture of cubic and, at a lesser extent, tetragonal phases similar to data reported in [8]. For Y-ZrO_2 powders with 15 mol.% Y_2O_3 calcined at high T_c (900 °C–1000 °C), broad Raman peaks were observed at about 275–280 cm^{-1} and 615–618 cm^{-1} that corresponds to cubic ZrO_2 phase. These findings are similar to those reported in [2, 38].

The Raman spectra of Cu-doped ZrO_2 powders prepared with low Cu loading (0.1–0.5 mol.% CuO) showed shapes similar to those of pure ZrO_2 counterparts. Significant Rayleigh scattering was detected and explained by the nanocrystalline nature of the powders. An increase of Cu loading up to 1 mol.% CuO resulted in the appearance of near-infrared luminescence in Cu-doped ZrO_2 powders. The increase of calcination temperature from 600 to 1000 °C enhances further this luminescence. This can be caused by the formation of copper-related luminescent centers sensitive to a 785-nm excitation light used for our Raman scattering experiment. This effect

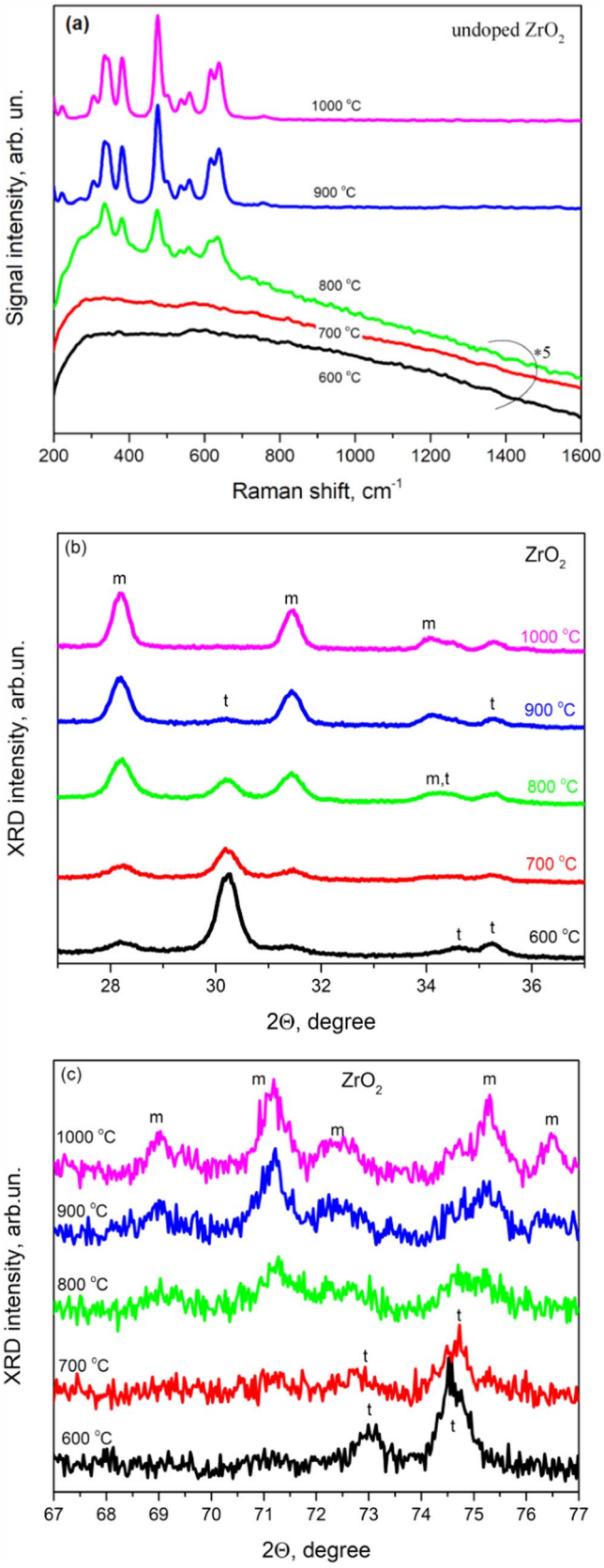

Figure 2. Raman scattering spectra (a) and XRD patterns (b) for pure ZrO_2 powders calcined at 600 °C–1000 °C during 2 h. In (a), the spectra for 600 °C–800 °C were multiplied by factor 5. In both figures the curves were shifted in vertical direction for clarity.

is the subject of another work and will not be discussed in detail here. Analysis of XRD patterns of Cu-ZrO_2 powders prepared low Cu loading (0.1–0.5 mol.% of CuO) revealed their similarity to those reported for pure ZrO_2 powders in figure 2. Calcination at T_c= 600 °C resulted in the formation of the *t*-ZrO_2 phase. This

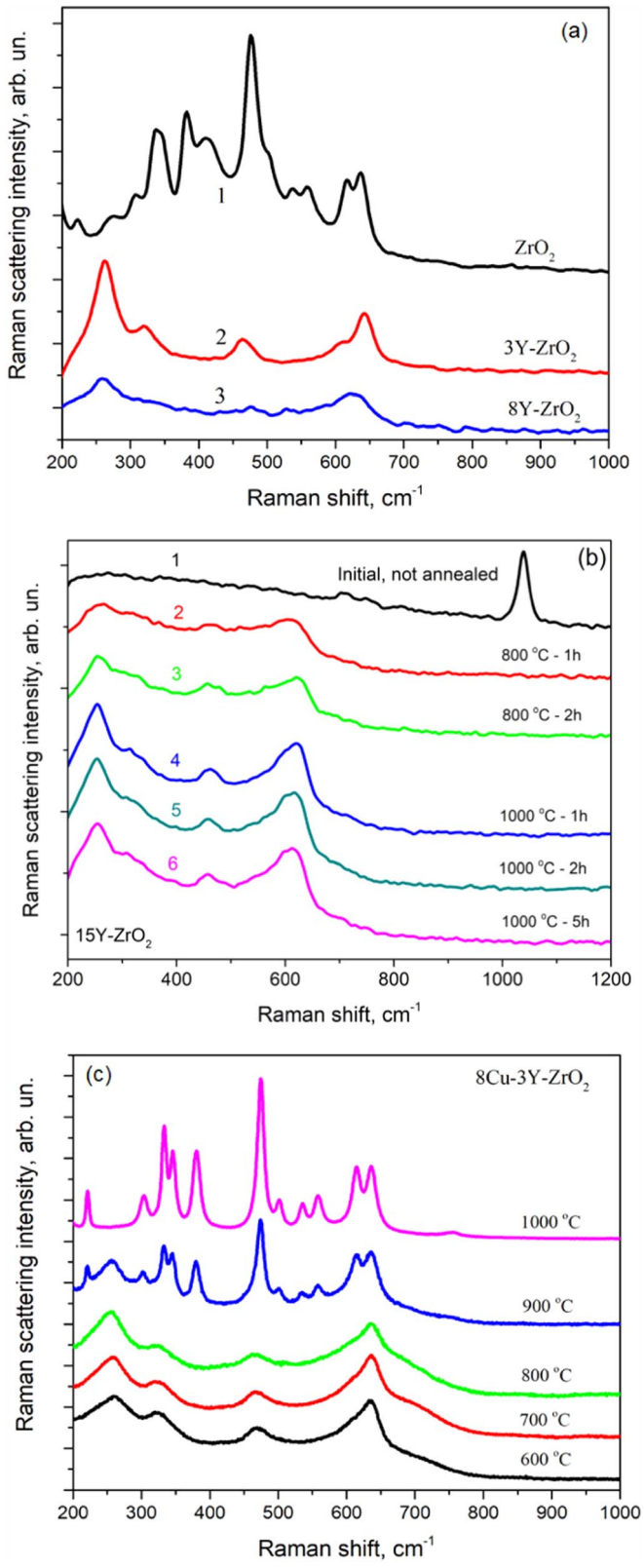

Figure 3. Raman scattering spectra for: (a) pure ZrO_2 (1) and Y-doped ZrO_2 (2,3) powders calcined at 1000 °C for 2 h, with Y content of 3 mol.% Y_2O_3 (2) and 8 mol.% Y_2O_3 (3); (b) Y-doped ZrO_2 powders calcined at 800 °C (1,2) and 1000 °C (3–5) during 1 h (1,3), 2 h (2,4) and 5 h (5), with Y content of 15 mol.% Y_2O_3; (c) (Cu,Y)-codoped ZrO_2 powders calcined at 600 °C–1000 °C for 2 h, with Cu and Y content of 8 mol.% CuO and 3 mol.% Y_2O_3, respectively. The spectra in the figures were vertically shifted for clarity.

statement is supported by TEM and EDX examination of these powders. A high-resolution TEM image of few powder grains lying on the holey carbon film of a TEM copper grid is shown in figure 4(a). Some crystalline grains with the sizes of 8–12 nm can be seen. STEM EDX images for the distribution of oxygen (figure 4(b)),

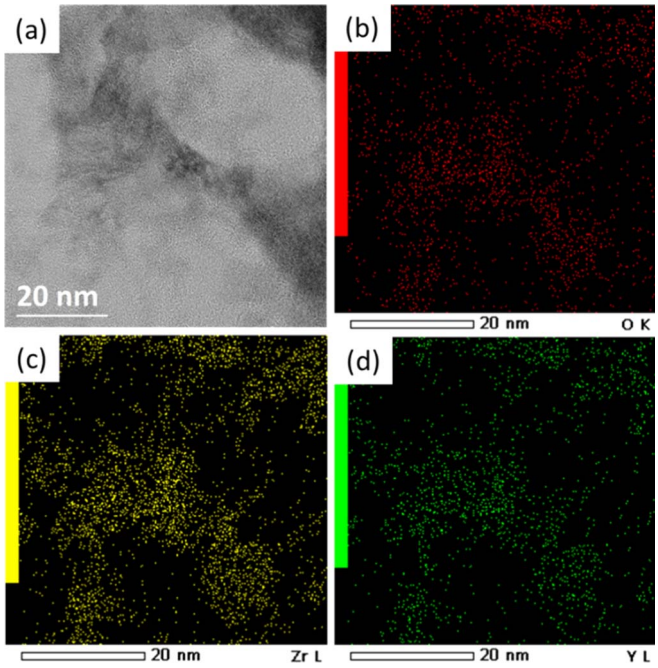

Figure 4. High-resolution TEM image of the few grains in Y-doped ZrO_2 powder (a) and STEM-EDX (b)–(d) chemical maps recorded for oxygen (b), zirconium (c) and yttrium (d).

zirconium (figure 4(c)) and yttrium (figure 4(d)) elements were recorded. The comparison of these chemical maps revealed the uniform distribution of yttrium dopant in zirconium dioxide grains.

Annealing of Cu-ZrO_2 powders at higher temperatures causes the grain growth and structural transformation to the monoclinic phase (figure 3). This phenomenon is significant for the powders with high Cu content (8 mol. % CuO). This transformation occurs via Cu outward diffusion from the grain volume to their surface and formation of CuO inclusions. These latter can be revealed in Raman spectra via the presence of the phonons appearing in the interval of 269–296, 316–343 and 604–627 cm^{-1} [39] which positions shift to the higher wavenumbers for powders with larger grains. The formation of crystalline CuO phase was also indicated by XRD study showing CuO related peaks at $2\theta \sim 68^{\circ}$ [37] as well as at $2\theta \sim 35.5$ and 46.4° [39].

The Raman study of (Cu,Y)-ZrO_2 powders revealed the presence of the tetragonal phase, which remained stable up to 1000 °C for powders with 3 mol.% Y_2O_3 and 0.1–1.0 mol.% CuO. However, the increase in Cu loading led to the destabilization of this phase. Although for $T_c = 900$ °C the phonon mode peaked near 260 cm^{-1} is still present (figure 2(c)), the main contribution is given by the monoclinic phase indicating transformation of both *t*- and *c*-phases to the *m*-ZrO_2. This could be attributed to copper and, in large extent, yttrium out-diffusion from the grains. Similar results were described in the [31]. It was reported that the calcination at high T_c decreases the Cu content in the grains, facilitating its outward diffusion from the grain volume to the surface. Subsequently, this opens the 'channels' for Y out-diffusion, leading to the destabilization of *t*- and *c*-phases [31]. Thus, one can assume that similar mechanism of structural transformation can occur in the powders investigated here.

The TEM examination of (Cu,Y)-ZrO_2 powders in initial state revealed their amorphous nature. Calcination at 600 °C for 2 h results in crystallization and the formation of the tetragonal phase. For the powders with low Cu content (0.1 mol.% CuO) the grain sizes were found to be similar to those in figure 4. For higher Cu loading (0.2 mol.% CuO), the grain growth was also revealed by TEM examination.

Figure 5(a) shows a selected area electron diffraction (SAED) pattern of a region containing tens of grains. The diffraction rings fit perfectly with the tetragonal phase of ZrO_2 with $a = b = 0.364$ nm and $c = 0.527$ nm. Its spatial group is $P4_2/nmc$. Figure 5(b) is a typical HRTEM image showing a tetragonal ZrO_2 grain along the [−101] direction. The average size of these grains is about $d = 15$ nm.

The structural characterization of the powders with higher Cu content (1–8 mol.% CuO) revealed a microstructure similar to that of the powders studied earlier and described in [37]. It turned out that with the T_c rise, the coherent domain sizes of ZrO_2 grains varied from $d \sim 8$ nm ($T_c = 600$ °C) up to $d \sim 15$ nm ($T_c = 1000$ °C), being smaller than in undoped powders. This indicates that the additional incorporation of copper results in the structural distortion and smaller coherent domain size. It is interesting that for higher Y content (8–15 mol.% Y_2O_3), both *t*- and *c*-phases were stable up to 1000 °C regardless of the Cu content. This

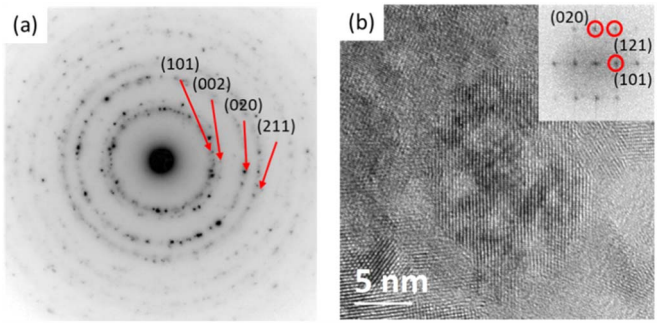

Figure 5. SAED image (a) and typical HRTEM image (b) of the (Cu,Y)-ZrO_2 powder (with 3 mol.%Y_2O_3 and 0.2 mol.%CuO) demonstrated a tetragonal structure of ZrO_2 grain along the [−101] direction.

suggests that the Y dopant plays a primary role in stabilizing the *t*- and *c*-phases of zirconia host. The transformation of structural and optical properties revealed the complexity of variations in powder properties when the ZrO_2 host is simultaneously doped with several additives.

3.2. UV–vis absorption spectra

To study the optical properties of the powders, the UV–vis diffuse reflectance method was used. The recorded diffuse reflectance spectra were converted to the absorption spectra using software associated with the setup. Their analysis was performed with the respect to dopant loading and calcination regimes.

3.2.1. Pure and Y-doped ZrO_2 powders

The UV–vis absorption spectra of pure ZrO_2 powders exhibit a typical broad band in UV spectral range centered near 300 nm and increasing in intensity towards the shorter-wavelength side. Sometimes a peak near 225 nm is detected [6, 29, 33]. The spectra of Y-doped powders have similar shape (figure 6). In initial state (just after drying) the broad band peaked near 290–300 nm is present (figure 6(a)) along with an increasing in intensity towards the shorter-wavelength side. For higher Y content, this band tends to broaden with a slight shift of its maximum down to 290 nm (figure 6). Additionally, the band near 240 nm can also be observed, in particular in powders with high Y loading (10–15 mol.% Y_2O_3). Taking into account that all the powders are amorphous in initial state, both bands can be ascribed to the Zr hydroxide and/or amorphous ZrO_2 powder, if any (figure 6(a)).

Powder calcination induces a transformation of the UV absorption band. The contribution of the 300-nm band decreases with an increase in calcination temperature, but some signal is still observable at 300–310 nm, becoming broader towards the longer-wavelength side (figure 6(a)). Additionally, the signal intensity increases towards deeper ultraviolet. As a result of powder calcination, which leads to their crystallization, the UV band peaked at 300–310 nm is considered to belong to crystallized ZrO_2. Typically, the bandgap of crystallized ZrO_2 exceeds 5.5 eV (~225.4 nm) [2], and therefore, it can be assumed that UV absorption is more likely caused by energy levels formed by some defects inside the bandgap of the ZrO_2 host than band-to-band absorption. For Y-doped ZrO_2 powders, the UV band has higher intensity for higher Y content. Since, Y-doping is accompanied by the formation of oxygen vacancies, the UV band one can ascribe to newly formed oxygen vacancies.

3.2.2. (Cu,Y)-ZrO_2 powders

The absorption spectra of Cu-doped powders consist of two main absorption bands (figure 7). One of them is a UV band, observed at about 300 nm and 230 nm, close to the ZrO_2 band edge in initial powders. This band is similar to the UV band described earlier for Y-doped ZrO_2 powders. An increase in Cu loading is accompanied by band broadening towards the longer-wavelength side, which may be caused by the appearance of additional oxygen vacancies due to charge compensation of the Cu dopants. Annealing of Cu-doped powders at 600 °C results in further broadening of the UV band, as well as in the shift of its peak position up to 380 nm (figure 4). The higher the Cu loading, the more pronounced this shift becomes. A comparison of absorption spectra for Cu-free and Cu-doped samples with the same Y content reveals that the observed behavior of the absorption spectra is attributed to Cu doping, i.e., its incorporation in ZrO_2 host and the formation of additional vacancies required for Cu charge compensation. This effect is considerable since the powders were synthesized from Zr, Y and Cu nitrates in present study.

One more absorption band was observed in the 500–1000 nm spectral range (figure 7). Its significant contribution was detected for the powders Cu content higher than 0.2 mol.% CuO. This band is broader, and its contribution increases with Cu content rise. This band can be ascribed to the *d-d* transitions of the Cu^{2+} ions. These ions can be situated in octahedral or tetragonal distorted octahedral surrounding and be associated with

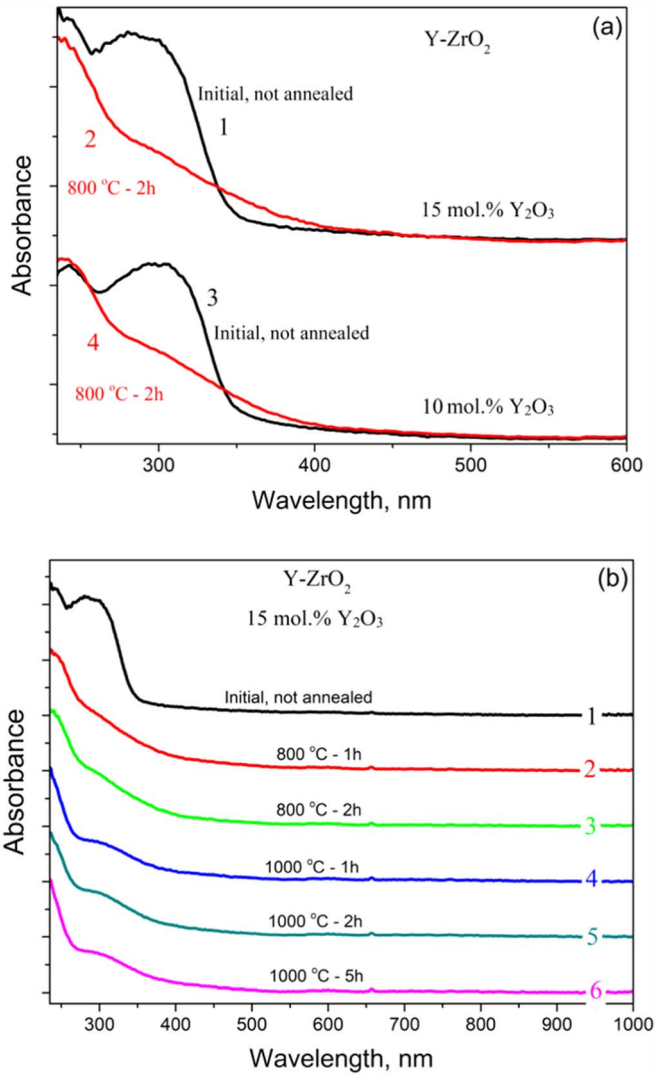

Figure 6. UV–vis absorption spectra of: (a) ZrO_2 powders doped with 10 (1,2) and 15 (3,4) mol.% of Y_2O_3, before (1,3) and after calcination at 800 °C for 2 h (2,4); (b) Y-doped ZrO_2 powder with 15 mol.% Y_2O_3 before (1) and after calcination at 800 °C (2,3) and 1000 °C (4–6) for 1 h (2,4), 2 h (3,5) and 5 h (6). The spectra were vertically shifted for clarity.

dispersed CuO on the grain surface or with Cu_{Zr}^{2+} substitutional atoms located in the near-surface region [6, 18, 19].

The absorption spectra of all Cu-doped powders calcined at 600 °C, and those with low Cu loading calcined at 800 °C demonstrate the similar shape (figure 7). The comparison of obtained results with those reported in the [38] permits to conclude that the powders with low Cu loading contain the grains covered by dispersed Cu_xO species. Since no signal from crystalline CuO was detected, one can assume that no deformation of CuO chains occurs. Based on the similarity of the spectra presented in [38–41] with those from present study, the Cu-related absorption band can be escribed rather to Cu_2O or Cu_xO than CuO species.

This indicates significant amount of extra-framework Cu sites and distinct nature of Cu_xO_y species present at the grain surface.

The spectra of (Cu,Y)-ZrO_2 powders with high Y loading (up to 10 mol.% Y_2O_3) also showed two main bands: one in the UV range related to oxygen vacancies and another CuO-related absorption in visible spectral range (figure 7(d)). The curves 4 and 6 in figure 7(c) and curve 2 in figure 7(d) have similar shape. This indicates that similar Cu_xO species can be observed on the ZrO_2 grain surface in such powders. This finding is supported by the examination of the same powders with electron paramagnetic resonance.

The EPR spectra were recorded for all powders and some of them, recorded for (Cu,Y)-codoped ZrO_2 powders, are depicted in figure 8. Generally, the powders in the initial state show clear asymmetric shape. This feature is indicative of surface Cu-related centers like Cu-OH. Similar spectra were reported in [29, 30]. The

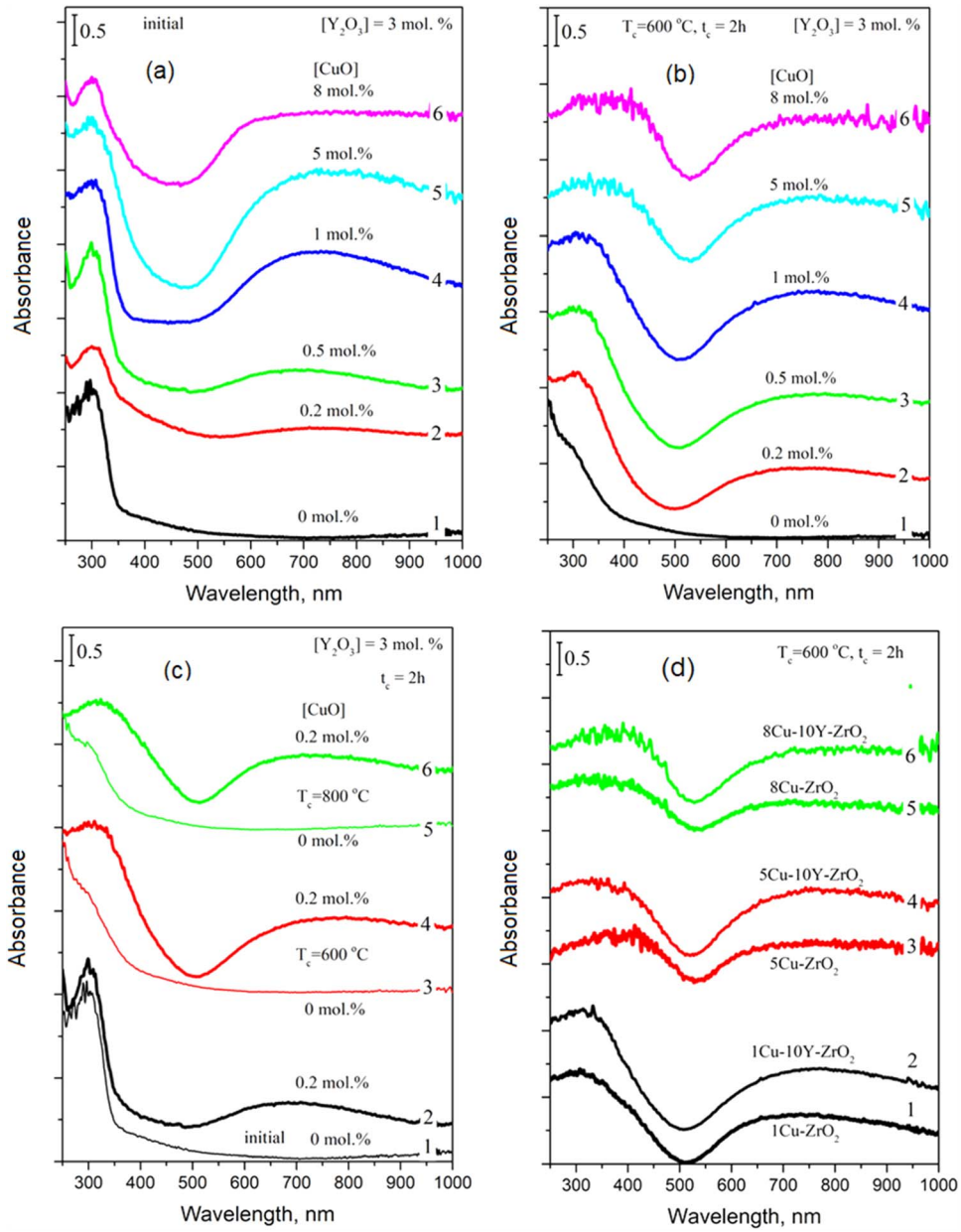

Figure 7. UV–vis absorption spectra of (Cu,Y)-ZrO_2 powders in initial state (a) and after calcination at 600 °C for 2 h (b); Cu content varies from 0 to 8 mol.% CuO; (c) effect of calcination temperature on optical absorption of Cu-free (1,3,5) and (Cu,Y)-ZrO_2 (2,4,6) powders in initial state (1,2) and after calcination at 600 (3,4) and 800 (5,6) °C for 2 h; (d) the effect of Cu content on optical absorption spectra of Y-free (1,3,5) and (Cu,Y)-ZrO_2 (2,4,6) powders calcinated at 600 for 2 h; the content of dopants is mentioned in the figure.

higher the Cu loading, the higher intensity of this signal becomes (figure 8(a)). Thus one can assume the increase of Cu content in the powders is accompanied by the increase in intensity of this signal.

The calcination of the powders at 600 °C for 2 h causes the transformation of EPR signal (figure 8(b)) that can be caused by the decomposition of some Cu-OH complexes or their reconstruction at the grain surface. The appearance of the signal related to Cu_{Zr}^{2+} defects is seen. This effect is more pronounced after calcination at 800 °C caused significant transformation of EPR signal. Its shape becomes nearly the same as that of the signal detected for Cu_{Zr}^{2+} site defects situated in monoclinic ZrO_2 [6]. At a glance, the parameters of observed EPR centers are similar to those reported in [6], however, this issue needs more study. At the same time, one can conclude that upon calcination at 800 °C for 2 h, a pronounced appearance of monoclinic phase in (Cu,Y)-ZrO_2 powders occurred. This is in the agreement with the Raman scattering data (figure 3).

Such powder transformation and redistribution of Cu and, consequently, Y dopants can stimulate the formation of additional phases. However, neither Raman scattering, nor TEM observation revealed the formation of such phases at 600 and 800 °C (figures 3–5). The distribution of chemical elements in these powders was studied with AES spectroscopy.

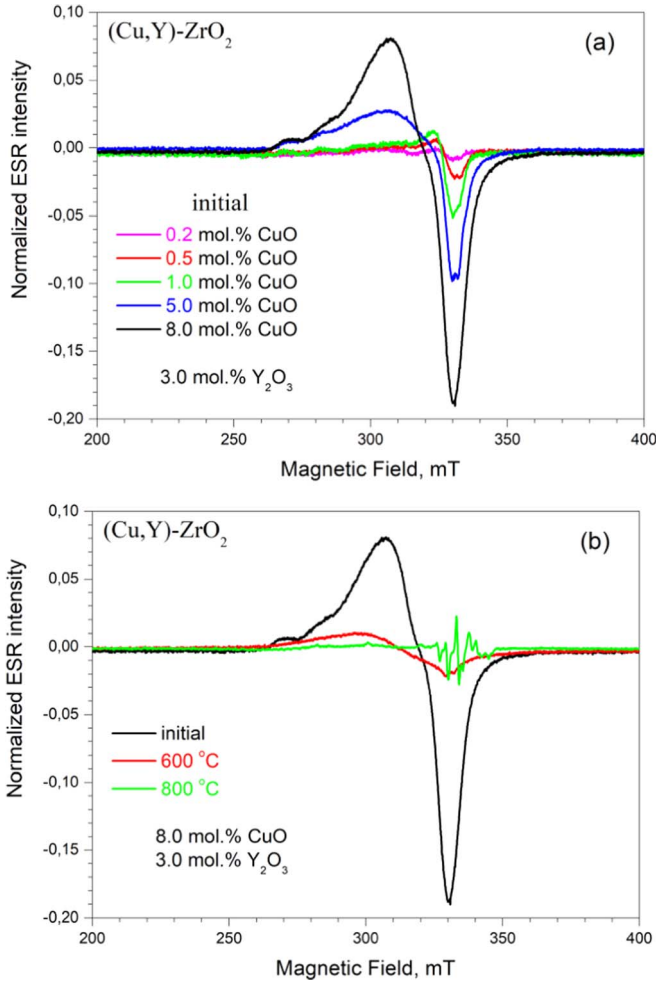

Figure 8. EPR spectra of novel (Cu,Y)-ZrO_2 powders recorded in initial state (a) and after calcination (b) for the samples with different Cu content mentioned in the figures. Y content was 3 mol.% Y_2O_3, being the same for (a) and (b).

The AES spectra of the (Cu,Y)-ZrO_2 powders (3 mol.% Y_2O_3 and 8 mol.% CuO) studied earlier, along with the AES spectra for the powders obtained in the present study are shown in figure 9. The Auger signals for O_{KLL} (around 509 eV), Cu_{LMM} (around 915 eV), Y_{LMM} (around 1746 eV), and Zr_{MNN} (around 141 eV) were analyzed.

It is worth to point out that the AES spectrum for reference (Cu,Y)-ZrO_2 powder (curve 1), investigated earlier using TEM, EDS, Raman scattering and XRD methods, shows no specific phases. The AES spectrum of the powder with the same chemical composition prepared in this work (curve 2) is similar to that of reference sample. The same similarity is seen for curve 3, however, Cu_{LMM} signal has lower intensity due to low Cu loading. Since the AES spectra are similar and, in this study, TEM observation revealed similar powder structures, it is hardly possible to expect the formation of different phases and substances than ZrO_2 grains doped with Cu and Y and/or covered with Cu_xO substances.

Analysis of the Cu_{LMM} AES signal showed that the Cu_{LMM} peak position is in the range of 909–916 eV where the peaks from metallic Cu, Cu_xO and Cu_2O species can be detected. Thus, one can assume that in our powders, Cu dopants present rather as surface complexes Cu_xO and Cu-OH than CuO. This conclusion is in agreement with results reported in [30, 39–41] as well as with EPR data and UV–vis absorption spectra.

We have performed analysis of the UV–vis absorption spectra of the powders using Tauc plot approximation. The spectra of all samples were transformed using $(\alpha h\nu)^n = f(h\nu)$ relationship. However, only for some powders, the linear behavior of this relationship in UV range was seen (figure 10). By extending the absorption edge to the energy axis, the bandgap value E_g was determined by extrapolating a straight line at $\alpha h\nu = 0$. It turned out that for most powders the bandgap value is in the range $E_g = 5.45$–5.65 eV. For the powders, which showed dependence similar to the curve 4 in figure 10, one can conclude that their bandgap exceeds 5.8 eV (detection limit of our setup). This can be a case for the powders with cubic structure that is known to demonstrate the largest bandgap among different ZrO_2 phases [6, 42].

Apart from this, pure ZrO_2 powders tend to demonstrate larger bandgap than their Y-doped and (Cu,Y)-codoped counterparts (figure 10, curves 1–3) that is in agreement with the results reported earlier [29, 43]. For

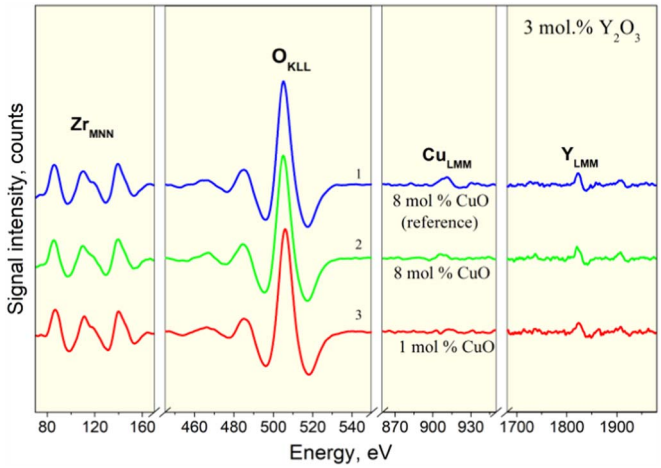

Figure 9. AES spectra (convoluted with a hardware function) for the reference (1) and novel (Cu,Y)-ZrO_2 (2,3) powders calcined at 600 °C for 2 h. Accelerating voltage – 10 kV, probe current – $5{\cdot}10^{-8}$ A.

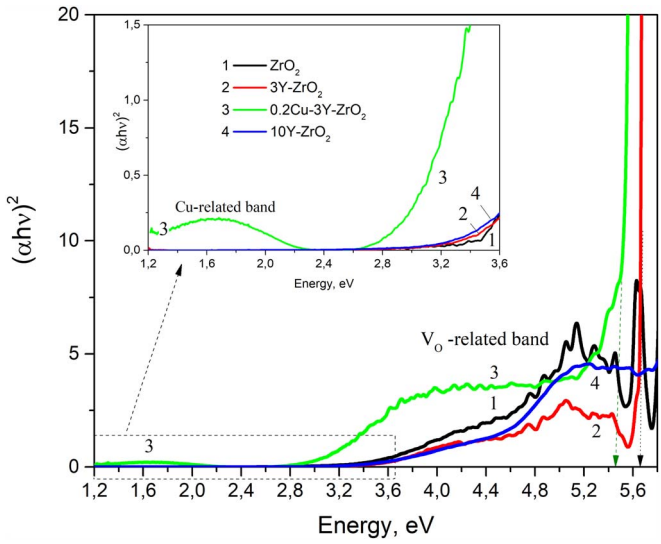

Figure 10. Tauc plot of UV–vis absorption spectra for the powders calcined at 600 °C for 2 h: 1 - pure ZrO_2, 2 - Y-ZrO_2 (3 mol.% Y_2O_3), 3 - (Cu,Y)-ZrO_2 (0.2 mol.% CuO and 3 mol.% Y_2O_3), and 4—Y-ZrO_2 (10 mol.% Y_2O_3).

the powders calcined at 800 °C–1000 °C, no linear relationship in UV spectral range was observed. However, for Y-doped ZrO_2 with high Y content, the cubic structure was detected assuming to enlarge the bandgap. In this regard, the plateau in the range of 5.2–5.8 eV (figure 10, curve 4) can be caused by the overlapping of several absorption bands, for instance, the contribution of $O\ 2p \rightarrow Zr\ 4d$ charge transfer transitions and newly formed host defects as oxygen vacancies or defect complexes. Besides, it can originate from the lowering of the coordination number of oxygen with zirconium. In doped materials, it is effectively 7 rather than 8 in pure tetragonal ZrO_2 that can also lead to some narrowing of the bandgap of doped tetragonal ZrO_2[43].

Thus, the study of UV–vis absorption spectra of (Cu,Y)-ZrO_2 powders allows assuming that the powders with a Cu loading of 1 mol.% CuO calcined at 600 °C and those with lower Cu loading (0.2–0.5 mol.% CuO) calcined at 600 and 800 °C show an intense Cu-related absorption band that is a signature of the presence of large amount of dispersed Cu_xO complexes at particle surface. Furthermore, due to Y doping, these particles exhibit stabilized *t*- and *c*-phases, which are known to show higher catalytic activity compared to *m*-ZrO_2. Additionally, these powders consist of small ZrO_2 particles ($d = 8$–15 nm) with large surface area and can hold promise for catalytic tests, for instance, for the CO-PROX reaction that are in progress.

3.3. Infrared reflection spectra

As mentioned earlier, Raman scattering is sensitive to crystal symmetry and has been successfully applied to characterize phase transformations in the ZrO_2 host. However, distinguishing the phonons for the *c*-ZrO_2 phase

Table 1. Self-consistent parameters for bulk ZrO_2 with different crystalline structure.

Parameters	ε_0	ε_∞	ν_T, cm^{-1} (γ_f, cm^{-1})	ν_L, cm^{-1} (γ_f, cm^{-1})
ZrO_2, cubic [45]	27	4.8	375 (10)	695 (10)
ZrO_2, tetragonal [46]	25	4.8	164 (97)	232 (119)
			339 (69)	354 (95)
			467 (106)	650 (139)
			580 (35)	581 (39)
			672 (172)	734 (113)
ZrO_2, monoclinic [47]	16	4.8	92 (130)	104 (260)
			330 (55)	381 (80)
			410 (20)	423 (28)
			480 (30)	515 (60)
			534 (100)	556 (138)
			570 (60)	615 (60)
			740 (110)	760 (120)

in a mixed-phase sample is challenging because they are broader compared to those of *m*- and *t*-ZrO_2. Additionally, for powders with smaller grains, Rayleigh scattering is significant and can dominate in Raman scattering spectra. In such cases, infrared reflection spectroscopy proves to be sensitive to both the structure of the powders and the nature of surface substances. Developing theoretical models for fitting experimental data can be helpful for characterizing nanopowders with mixed crystalline phases. In this section, we discuss the results obtained for the same powders using infrared reflection spectroscopy.

3.3.1. Theoretical models and spectra simulation

To model infrared reflection spectra of ZrO_2 powders, a mathematical model was built based on the frequency dependence of the dielectric constant given by the well-known Helmholtz–Kettler formula

$$\varepsilon(\nu) = \varepsilon_\infty + \sum_{i=1}^{n} \frac{\varepsilon_f \nu_i^2}{\nu_i^2 - \nu^2 + i\gamma_f \nu} \tag{1}$$

where ε_∞ is the high-frequency dielectric permittivity, ε_f is the contribution of active *i*-th phonon with the frequency ν_i and γ_f is corresponding damping coefficient, and ν is the frequency of infrared irradiation [44]. In other words, the dielectric constant can be presented as

$$\varepsilon(\nu) = \varepsilon_1 + i\varepsilon_2 = \varepsilon_\infty + \varepsilon_f, \tag{2}$$

and the reflection coefficient $RT(\nu)$ can be calculated as

$$RT(\nu) = \left[\frac{\sqrt{\varepsilon(\nu)} - 1}{\sqrt{\varepsilon(\nu)} + 1}\right]^2. \tag{3}$$

The simulation of the IR reflection spectra for different ZrO_2 phases in the range of 'residual rays' was performed using the formula (2) and taking into account the interaction of infrared radiation with the phonon subsystem only because of dielectric ZrO_2 nature. For the cubic ZrO_2 phase, a single-oscillator model was applied [45], while for tetragonal and monoclinic phases—five [46] and seven [47] oscillators were considered, respectively.

It is worth pointing out that, typically, the frequencies of different Zr-O and Zr-O-Zr vibrations are reported in the literature [20, 22, 32] while the damping coefficients of these phonons are less addressed [45–47].

Self-consisted parameters of the oscillators are presented in table 1. The value of static dielectric constant was determined from the Lydden–Sachs–Teller ratio [44]. The simulation was carried out using the Kramers–Kronig ratio.

By applying the developed mathematical model and considering the additive and phenomenological contribution of phonon subsystem into the dielectric permittivity, the infrared reflection spectra for different ZrO_2 phases were simulated (figures 11(a), (b)). Obtained results were found to be in a good agreement with experimental data reported in [45–47].

Analysis of the peculiarities of the theoretical spectra simulated for three ZrO_2 phases revealed a distinct minimum in the reflection spectra. This unique spectral feature can be used for the express identification of the crystalline phase. Specifically, a reflection minimum occurs at approximately 700–720 cm^{-1} for *c*-ZrO_2,

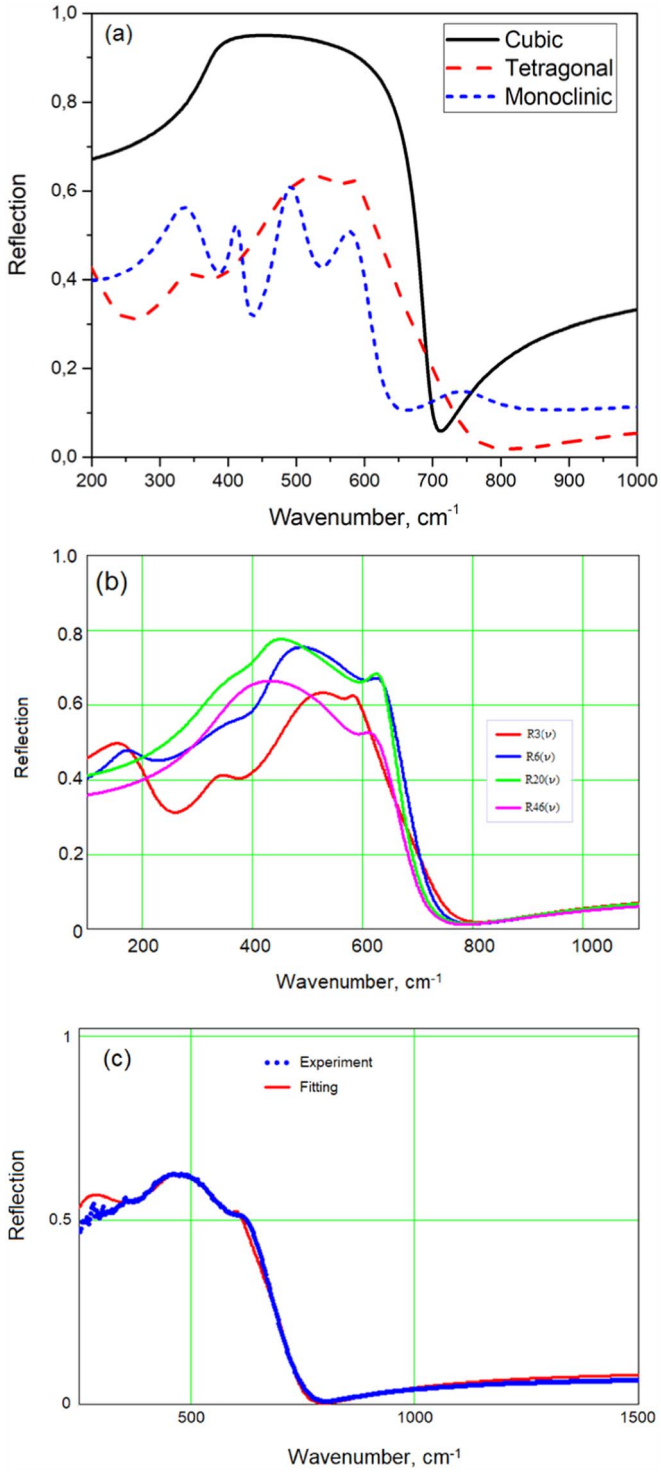

Figure 11. (a) Simulation of the IR reflection spectra using the parameters of phonon subsystem for the *m*-, *t*- and *c*-ZrO_2 phases from table 1; (b) Modelling of IR reflection spectra for Y-doped ZrO_2 with 3, 6, 20 and 46 mol.% of Y_2O_3; (c) experimental spectrum for tetragonal 3Y-ZrO_2 sample (blue symbols) and its fitting (red line).

790–800 cm^{-1} for *t*-ZrO_2 and 820–840 cm^{-1} for *m*-ZrO_2 phase. In addition, the simulation of the spectra revealed minimal effect of phonon damping coefficient γ_f on the spectral position of the reflection minimum for each phase.

This approach was initially employed to fit an experimental spectrum obtained for a Y-doped ZrO_2 sample (with 3 mol.% Y_2O_3) (figure 11(c)). The reflection minimum position is around 800 cm^{-1}. To fit this spectrum, a five-oscillator model and self-consistent parameters, collected in table 2, were used. The result is present in figure 11(c) by the red curve, showing good agreement with experimental data. However, the best match was achieved when additional oscillator (with the frequency ~375 cm^{-1}) was included. Finally, the fitting indicated

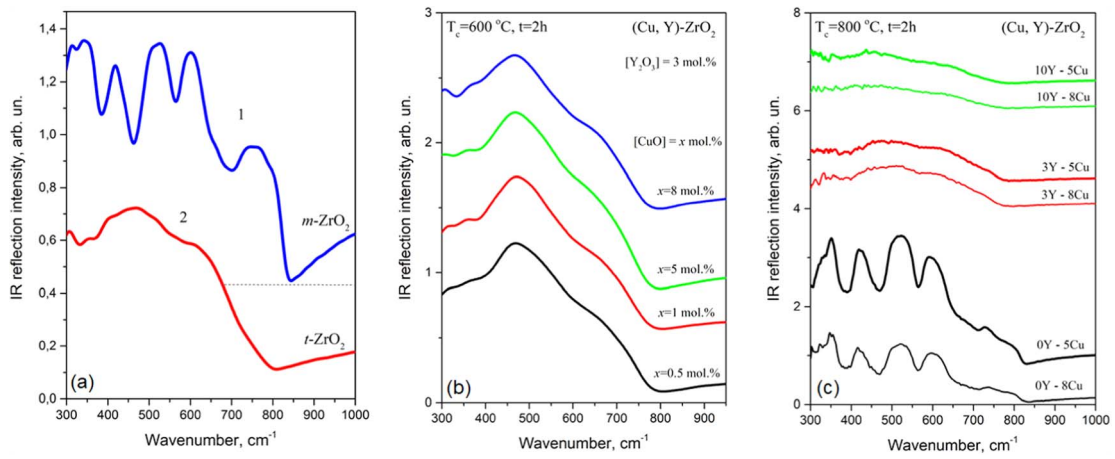

Figure 12. Experimental IR reflection spectra of (a) ZrO_2 (1) and 3Y-ZrO_2 (2) calcined at 600 °C for 2 h; (b,c) (Cu,Y)-ZrO_2 powders calcined at 600 °C (b) and 800 °C (c) for 2 h; Cu and Y loading are mentioned in figures. The spectra are shifted vertically for clarity.

Table 2. Self-consistent parameters for fitting of experimental data.

Spectrum	ε_0	ε_∞	ν_T, cm^{-1} (γ_β cm^{-1})	ν_L, cm^{-1} (γ_β cm^{-1})
Figure 11(c) (mixture of tetragonal and cubic phases)	25	4.8	164 (2)	232 (2)
			339 (120)	354 (110)
			450 (70)	666 (130)
			600 (35)	601(39)
			672 (140)	734 (80)
			375 (150)[a]	

[a] the additional phonon is employed to fit experimental data.

that the primary phase is tetragonal, while some distortion of tetragonal lattice, for instance, due to dopants, cannot be ruled out.

3.3.2. Analysis of experimental IR reflection spectra

The spectra were recorded and analyzed for all powders. Figure 12 shows the spectra for the pure doped ZrO_2 powder (curve 1) and Y-doped ZrO_2 powder (curve 2). The corresponding XRD data are shown in figure 2. By comparing experimental and theoretical IR spectra, we can establish the correlation between crystalline structure and shape of the IR reflection spectra can be obtained and employed for further analysis.

As shown in figure 12(b), the spectra of the (Cu,Y)-codoped ZrO_2 powders calcined at 600 °C are similar regardless of Cu loading. The broad peak at about 450 cm^{-1} and shoulders near 360–380 cm^{-1} and 660–680 cm^{-1} are clearly visible (figure 12(b)). The spectral position of the reflection minimum is about 800 cm^{-1}. In contrast, the spectra in figure 12(c) demonstrate significant shift of minimum position towards the lower wavenumbers with increasing Y content in the powders. Indeed, starting from about 830 cm^{-1} for Y-free powder it shifts towards 770 cm^{-1} for 3 mol.% Y_2O_3 and remains nearly the same for 10 mol.% Y_2O_3 (figure 12(c)). The change in spectrum shape also indicates a structural transformation from monoclinic ZrO_2 to tetragonal one. It is worth to point out that the effect of the Cu loading on such transformation is negligible. These findings support our statement regarding the main role of Y dopant in formation of tetragonal (cubic) structure of doped ZrO_2, which remains stable at elevated calcination temperatures.

Figure 12(c) shows that IR reflection spectra of Cu-ZrO_2 powders calcined at 800 °C are similar to those of *m*-ZrO_2 (figure 12(a)). Consequently, the Cu-ZrO_2 powders calcined at 800 °C have mainly monoclinic structure while the increase in Cu loading leads to the broadening of the vibration modes. The results support also the EPR data, showed the formation of Cu_{Zr}^{2+} defects in monoclinic structure. Based on the results described in this section, one can conclude that the developed models for simulating IR reflection spectra give a hand to determine the type of crystalline structure of the powders (both for single and mixed-phase cases) as well as to track structural transformation caused by the doping and/or thermal treatment.

4. Conclusions

This study had two primary objectives: to investigate the effect of Cu and/or Y dopant content and calcination regimes on the structural and optical properties of Cu-ZrO_2, Y-ZrO_2 and (Cu,Y)-ZrO_2 nanopowders, and to develop an approach that integrates various optical methods for express monitoring of powder properties. Undoped and doped ZrO_2 nanopowders were synthesized using a co-precipitation method with Zr, Y and Cu nitrates. The dopant content was varied across a wide range (0.1–8.0 mol.% of CuO and 3–15 mol.% of Y_2O_3). The powders underwent calcination at temperatures ranging from 400 to 1000 °C for durations of 1, 2 and 5 h in an air atmosphere, followed by analysis using different methods. Comparing the results obtained for Y-ZrO_2, Cu-ZrO_2 and (Cu,Y)-ZrO_2 powders revealed that both impurities stimulates the appearance of additional oxygen vacancies in the powders. However, the formation of the tetragonal and cubic ZrO_2 phases is primarily influenced by Y content, regardless of the Cu loading. It was found that the powders with 0.2–1.0 mol.% CuO content and calcined at 600 °C, exhibited tetragonal grains with the sizes of about 8–10 nm and dispersed Cu_xO species on their surface, which may be attractive for catalytic applications. Calcination at higher temperatures resulted in grain growth (up to about 15 nm), reduced surface area, the formation of crystalline CuO, and appearance of Cu_{Zr}^{2+} site defects in monoclinic Zro2 phase. The bandgap value of the powders was found to be in the range 5.45–5.65 eV. Doping with Cu and Y results in the appearance of additional oxygen vacancies that form energy levels inside bandgap and manifest in the absorption spectra as UV band with peak position around 300–320 nm (3.8–4.1 eV). The Y-ZrO_2 powders with high Y content (8 mol.% Y_2O_3 and higher) calcined at elevated temperatures show a cubic structure with the bandgap larger than 5.8 eV. Additionally, this study demonstrated the effectiveness of developed theoretical models for identification of different ZrO_2 crystalline phases by means of infrared reflection spectroscopy. For cubic, tetragonal and monoclinic phases, theoretical models with one, five and seven oscillators were built, respectively. Simulated theoretical spectra revealed a distinct position of the high-frequency reflection minimum, correspondingly observed at 700–720 cm^{-1}, 790–800 cm^{-1} and 820–840 cm^{-1} for cubic, tetragonal and monoclinic phases. This unique feature for each crystalline phase depends only slightly on phonon damping coefficients. By comparing experimental and theoretical reflection spectra, the parameters of various phonons were determined. Additionally, the potential for identifying single and mixed-phase ZrO_2 structures was demonstrated. Integrating the aforementioned methods, an approach for monitoring powder properties is proposed, aiding in understanding the characteristics of ZrO_2 powders doped with several impurities and predicting their catalytic behavior.

Acknowledgments

This work was supported by the National Research Foundation of Ukraine from the state budget, project 2020.02/0380 «Structure transformation and non-equilibrium electron processes in wide bandgap metal oxides and their solid solutions» as well as by the National Academy of Sciences of Ukraine (projects III-10-21 and III-10-24). All the TEM results reported in this manuscript fall within the scope of the research foundation IRMA (FR 3095).

Data availability statement

The data cannot be made publicly available upon publication due to legal restrictions preventing unrestricted public distribution. The data that support the findings of this study are available upon reasonable request from the authors.

ORCID iDs

L Khomenkova https://orcid.org/0000-0002-5267-5945
O Isaieva https://orcid.org/0000-0003-1313-5409
O Melnichuk https://orcid.org/0000-0002-6768-8765
N Korsunska https://orcid.org/0000-0002-4778-5074

References

[1] Asadikiya M and Zhong Y 2018 *J. Mater. Sci.* **53** 1699
[2] Wang Y, Zhu Z, Ta S, Cheng Z, Zhang P, Zeng N, Goodman B A, Xu S and Deng W 2022 *Crystals* **12** 1081
[3] Gautam C, Joyner J, Gautam A, Rao J and Vajtai R 2016 *Dalton Trans.* **45** 19194
[4] Guo H, Bayer TJM, Guo J, Baker A and Randall C A 2017 *Scr. Mater.* **136** 141

[5] Lehninger D, Honeit F, Rafaja D, Klemm V, Röder C, Khomenkova L, Schneider F, von Borany J and Heitmann J 2022 *MRS Bull.* **47** 773
[6] Korsunska N and Khomenkova L 2018 Multifunctional Zirconia-based Nanocomposites *Solid State Composites and Hybrid Systems: Fundamentals and Applications* 1st edn, ed R Savkina and L Khomenkova (CRC Press) Ch 2 28–57
[7] Mosavari M, Khajehhaghverdi A and Mehdinavaz Aghdam R 2023 *Inorg. Chem. Commun.* **157** 111293
[8] Gazzoli D, Mattei G and Valigi M 2007 *J. Raman Spectrosc.* **38** 824
[9] Xue Q, Huang X, Wang L, Dong J, Xu H and Zhang J 2017 *Mater. Des.* **114** 297
[10] Wang W, Qu Z, Song L and Fu Q 2020 *J Catalysis* **382** 129
[11] Tadokoro S K and Muccillo E N S 2002 *J Alloys Compound* **344** 186
[12] Alvarez M R, Landa A R, Otero-Diaz L C and Torralvo M J 1998 *J. Eur. Ceram. Soc.* **18** 1201
[13] Park K, Yoon S J and Pi J W 2017 *Dyes Pigm.* **143** 317
[14] Smits K, Sarakovskis A, Grigorjeva L, Millers D and Grabis J 2014 *J. Appl. Phys.* **115** 213520
[15] Korsunska N, Baran M, Papusha V, Lavoryk S, Marchylo O, Michailovska K, Melnichuk L, Melnichuk O and Khomenkova L 2019 *Appl. Nanosci.* **9** 965
[16] Insoo R, Liu Y, Ball M R, Jackson D H K, Chada J P, Sener C, Kuech T F, Madon R J, Huber G W and Dumesic J A 2016 *ACS Catal.* **6** 7040
[17] Tada S H, Katagiri A, Kiyota K, Honma T, Kamei H, Nariyuki A, Uchida S and Satokawa S H 2018 *J. Phys. Chem.* C **122** 5430
[18] Samson K, Śliwa M, Socha R P, Góra-Marek K, Mucha D, Rutkowska-Zbik D, Paul J-F, Ruggiero-Mikołajczyk M, Grabowski R and Słoczyński J 2014 *ACS Catal.* **4** 3730
[19] Pakharukova V P, Moroz E M, Kriventsov V V, Larina T V, Boronin A I, Dolgikh L Y and Strizhak P E 2009 *J. Phys. Chem.* C **113** 21368
[20] Štefanic G, Musić S, Popović S and Furić K 1996 *Croat. Chem. Acta* **69** 223
[21] Schäfer H, Brandt S, Milow B, Ichilmann S, Steinhart M and Ratke L 2013 *Chem Asian* J **8** 2211
[22] Najafi A, Sharifi F, Mesgari-Abbasi S and Khalaj G 2022 *Ceram International* **48** 26725
[23] Gorban O, Danilenko I, Gorban S, Volkova G, Glazunova V and Konstantinova T 2017 *Photochem. Photobiol. Sci.* **16** 53
[24] Singhania A and Gupta S M 2017 *Beilstein J. Nanotechnol.* **8** 1546
[25] Asadi S, Abdizadeh H and Vahidshad Y 2012 *J Nanostruct* **2** 205
[26] Winnubst L, Ran S, Speets E A and Blank D H 2009 *J. Eur. Ceram. Soc.* **29** 2549
[27] Smits K, Olstains D, Zolotarjovs A, Laganovska K, Millers D, Ignatans R and Grabis J 2017 *Sci. Rep.* **7** 44453
[28] Hu Z, Wang Q, Liu J, Liu K, Zhang W, Yang Y, Wang Y and Chang Q 2021 *J Alloys Compounds* **856** 157397
[29] Gopal R, Sambandam A, Kuppulingam T, Meenakshisundaram S, AlSalhi M S and Devanesan S 2020 *J. Mater. Sci., Mater. Electron.* **31** 7232–46
[30] Korsunska N, Polishchuk Y, Baran M, Nosenko V, Vorona I, Lavoryk S, Ponomaryov S, Marie O, Portier X and Khomenkova L 2018 *Frontiers in Materials* **23** 5
[31] Marie O, Portier X, Korsunska N and Khomenkova L 2020 *Appl Catal B Environ* **278** 119258
[32] Gao Y F, Masuda Y, Yonezawa T and Koumoto K 2002 *J. Ceram. Soc. Jpn.* **110** 379
[33] Gao Y, Masuda Y, Ohta H and Koumoto K 2004 *Chem. Mater.* **16** 2615
[34] Anastassakis E, Papanicolaou B and Asher I M 1975 *J Phys Chem Sol* **36** 667
[35] Hirata T, Asari E and Kitajima M 1994 *J Sol St Chem* **110** 201
[36] Torres D I and Llopis J 2009 *Superlatt Microstruct* **45** 482
[37] Korsunska N, Polishchuk Y, Kladko V, Portier X and Khomenkova L 2017 *Mater. Res. Express* **4** 035024
[38] Zhao Y, Xu L, Guo M, Li Z, Xu Z, Ye J, Li W and Wei S 2022 *J Mater Res Technol* **19** 4003
[39] Poulston S, Parlett P M, Stone P and Bowker M 1996 *Surf. Interface Anal.* **24** 811
[40] Ganga B G, Carleschi E, Doyle B and Santhosh P N 2023 *Mater. Sci. Eng.* B **292** 116412
[41] Pan J, Yang C and Gao Y 2016 *Sensors Mater.* **28** 817
[42] French R H, Glass S J, Ohuchi F S, Xu Y N and Ching W Y 1994 *Phys. Rev.* B **49** 5133
[43] Aita C R, Hoppe E E and Sorbello R S 2003 *Appl. Phys. Lett.* **82** 677
[44] Melnichuk O V, Korsunska N O, Markevich I V, Boyko V V, Polishchuk Yu O, Tsybrii Z F, Melnichuk L Yu, Venger Ye F, Kladko V P and Khomenkova L Yu 2021 *Semicond Phys, Quantum Electron Optoelectron* **24** 390
[45] Feinberg A and Perry C H 1981 *J Phys Chem Sol* **42** 513
[46] Pecharromán C, Ocaña M and Serna C J 1996 *J. Appl. Phys.* **80** 3479
[47] Perry C H, Lu F, Liu D W and Alzyab B 1990 *J. Raman Spectrosc.* **21** 577